Dalton Transactions

ROYAL SOCIETY OF CHEMISTRY

PAPER

View Article Online
View Journal

Cite this: DOI: 10.1039/d4dt00904e

Substituent effects on spin-crossover Fe(II)N_4O_2 pyrenylhydrazone complexes†‡

Xuan Wang, Nan Zhang and Hui-Zhong Kou *

Received 27th March 2024,
Accepted 17th July 2024

DOI: 10.1039/d4dt00904e

rsc.li/dalton

Multifunctional magnetic materials have broad application prospects in molecular switches and information storage. In this study, four mononuclear Fe(II) complexes are synthesized using a series of pyrenylhydrazone ligands HL^{1-4}. Two deprotonated ligands are coordinated to the iron(II) ions in an enolic form, leading to neutral complexes $Fe^{II}(L^x)_2$·*xsol* with a $Fe^{II}N_4O_2$ octahedral coordination environment. Magnetic measurements suggest that complex $Fe(L^1)_2$·**2ACE** (**1·2ACE**, ACE = acetone) is mainly low spin below 300 K and complex $Fe(L^3)_2$·ACE (**3·ACE**) is high spin, whereas complexes $Fe(L^2)_2$ (**2**) and $Fe(L^4)_2$·$6H_2O$ (**4·6H_2O**) exhibit gradual spin crossover behavior. The spin states of complexes **1–4** are confirmed by single-crystal X-ray diffraction analysis. The substituent effect on the magnetic properties of the complexes is significant in this system. Temperature-dependent fluorescence emission spectra show the coexistence but no coupling effect of spin crossover and fluorescence for complexes **2** and **4·6H_2O**.

Introduction

Molecular magnetic materials, one of the research hotspots in coordination chemistry, can be widely used in the fields of information storage, photomagnetic and electromagnetic materials. Spin crossover (SCO) complexes have been an important research object among these materials in recent years.[1] When coordinated to ligands with moderate field strengths, $3d^4$–$3d^7$ transition metal ions can undergo reversible transitions of spin states in response to changes in external conditions, such as temperature, pressure and guest molecules.[2–4] The spin-state transitions accompanied by reversible changes in structural, magnetic and optical properties exhibit promising application value.[5–7]

With the development of spin-crossover systems with new structures and properties, the coupling effect between spin-crossover behavior and other physicochemical properties has become an important research target for researchers.[8–10] As a kind of multifunctional magnetic material, spin crossover–fluorescence bifunctional complexes have broad application prospects in molecular switches and molecular sensors.[11,12] The advantage of these materials is that they provide a way for the adjustment of fluorescence emission and an optical signal for the spin state switching of transition metal ions in the material.[13–17]

However, these complexes have strict requirements for the properties of ligands, which makes the design, synthesis and application of the materials challenging. To date, there are relatively few materials reported to achieve the coupling effect between spin-crossover and fluorescence properties, and some of them lack unambiguous structures.[18–21]

Pyrene is a typical fluorophore with a planar rigid conjugated structure. In recent years, it has also been applied in the construction of fluorescent spin crossover materials.[18,20,22–27] Herein we synthesized pyrene derivatives HL^{1-4} with a Schiff base structure (Scheme 1), which potentially produce fluorescent spin crossover Fe(II)N_4O_2 complexes.[13] And we attempted to adjust the magnetic and fluorescence properties of the complexes by changing the substituents on the ligands.

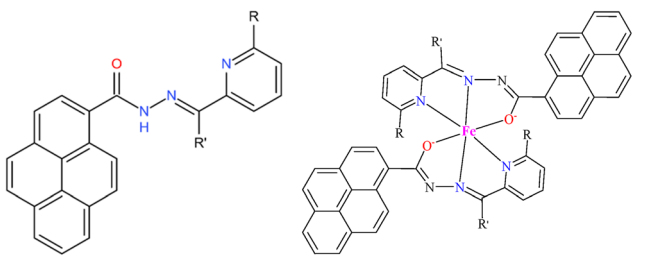

Scheme 1 Structure of ligands HL^1 (R = R′ = H), HL^2 (R = CH_3, R′ = H), HL^3 (R = Br, R′ = H) and HL^4 (R = R′ = CH_3) and the corresponding Fe(II) complexes.

Engineering Research Center of Advanced Rare Earth Materials (Ministry of Education), Department of Chemistry, Tsinghua University, Beijing 100084, P. R. China. E-mail: kouhz@mail.tsinghua.edu.cn

† Dedicated to Prof. Osamu Sato on the occasion of his 60th birthday.

‡ Electronic supplementary information (ESI) available: IR spectra, PXRD, TGA and detailed crystal structure. CCDC 2338645–2338650. For ESI and crystallographic data in CIF or other electronic format see DOI: **https://doi.org/10.1039/d4dt00904e**

Experimental section

All reagents were commercially available and used without further purification.

Synthesis

Synthesis of ligands. Precursor 1-pyrenecarbohydrazide was synthesized starting from 1-pyrenecarboxylic acid according to the literature method.[28]

HL^1 was obtained by the condensation reaction of 1-pyrenecarbohydrazide with pyridine-2-carboxaldehyde. To 1-pyrenecarbohydrazide (5.0 mmol, 1.3 g) in methanol (60 mL) was added an equivalent amount of pyridine-2-carboxaldehyde and a few drops of glacial acetic acid were added under stirring conditions. The solution was heated and refluxed at 65 °C for 8 h, then a faint yellow solid was obtained after cooling, filtration and drying.

Similarly, the ligands HL^2, HL^3 and HL^4 were obtained by replacing pyridine-2-carboxaldehyde with 6-methylpyridine-2-carbaldehyde, 6-bromopyridine-2-carbaldehyde and 6-methyl-2-acetylpyridine, respectively.

Synthesis of the complexes. HL^1 (37.3 mg, 0.1 mmol) was suspended in acetone (10 mL), then an aqueous solution of Et_4NOH (0.1 mmol) was added with stirring. To the resultant yellow solution, $Fe(ClO_4)_2{\cdot}6H_2O$ (18.1 mg, 0.05 mmol) in acetone (5 mL) was added dropwise. The solution became dark green, and stirring was continued for 30 min and then the solution was filtered. Slow diffusion of diethyl ether to the filtrate at room temperature led to green needle-like crystals of complex **1·2ACE** in about two days. Complexes **2·2ACE** and **3·2ACE** were similarly prepared by replacing HL^1 with HL^2 and HL^3, respectively. Complex **4·6H$_2$O** was similarly prepared by using HL^4 in acetonitrile instead of acetone.

Measurements

IR absorption spectra (KBr pellets) were recorded in the range of 4400–400 cm^{-1} on a WQF-510A FT-IR spectrophotometer. Variable temperature magnetic susceptibility measurements were performed on a Quantum Design MPMS-XL7 SQUID magnetometer. The experimental susceptibilities were corrected for the diamagnetism of the constituent atoms (Pascal's tables). Solid-state emission spectra were recorded on an Edinburgh FLS 920 fluorescence spectrophotometer. Powder X-ray diffraction (XRD) was performed using Cu Kα radiation (λ = 1.5418 Å) on a Rigaku diffractometer. Thermogravimetric analyses (TGA) were performed on a DTU-3A simultaneous thermal analyzer under a nitrogen atmosphere at a heating rate of 10 °C min^{-1}. Single crystal X-ray diffraction data were collected on a Rigaku SuperNova, Dual, Cu at zero, AtlasS2 diffractometer. The structures were solved by direct methods and refined using full-matrix least squares (SHELXL-2018 or Olex2 1.3) on F^2.

Results and discussion

Synthesis

The single crystals of complexes **1·2ACE–3·2ACE** can only be obtained by slow diffusion of ether to the acetone reactant solution, whereas for complex **4·6H$_2$O**, acetonitrile is the most suitable for single crystal growth. It is worth mentioning that tetraethylammonium hydroxide Et_4NOH, should be used to deprotonate the ligands, otherwise, high spin complexes $[Fe(HL^x)_2](ClO_4)_2$ would be obtained. The powder XRD patterns of complexes **2·2ACE** and **3·2ACE** do not match perfectly with those calculated from their single-crystal X-ray diffraction data. The acetone molecules in the crystal samples may affect their stabilities. The thermogravimetric analysis (TGA) results show that complex **1·2ACE** had a 13% weight loss at around 100 °C, corresponding to two acetones per molecule. As for complex **3·2ACE**, the weight loss from room temperature to 50 °C corresponds to approximately one acetone molecule, suggesting that the complex has partially desolvated to form **3·ACE**. No weight loss was observed in the thermogravimetric curve of complex **2·2ACE** (Fig. S1, ESI‡). This indicates that **2·2ACE** has undergone complete solvent loss at room temperature. Therefore, the solid samples of **2·2ACE** and **3·2ACE** used for magnetism and fluorescence measurements should be $Fe(L^2)_2$ (**2**) and $Fe(L^3)_2{\cdot}$ACE (**3·ACE**). The PXRD pattern of complex **4·6H$_2$O** coincides well with that calculated, which indicates a good structural stability of complex **4·6H$_2$O** at room temperature (Fig. S2, ESI‡). Complex **4·6H$_2$O** shows 12% mass loss before 200 °C in thermogravimetric analyses (Fig. S1, ESI‡), corresponding to six water molecules per formula unit. The further mass loss above 200 °C is due to the decomposition of the complex. The IR spectra of ligands HL^{1-4} and the complexes (Fig. S3, ESI‡) show that the peaks of the four complexes are similar due to their similar structure. The strong absorption peak at 1650 cm^{-1} for the C=O stretching vibration of free ligands HL^{1-4} disappears in the complexes, suggesting a transformation from the ketone to the enolic form for the ligands owing to the coordination. It is worth noting that there is no strong peak at around 1100 cm^{-1} for perchlorate in the complexes, which is consistent with the formation of the neutral iron(II) complexes.

Crystal structures

The crystal structures of complexes **1·2ACE** and **3·2ACE** at 173 K, complex **2·2ACE** at 100 K and 173 K, and complex **4·6H$_2$O** at 100 K and 220 K were investigated by single-crystal X-ray diffraction. The structural details of complexes are listed in Table 1, and selected bond lengths and bond angles are given in Table 2. The metric distortion parameter Σ (the sum of the deviation from 90° of the 12 *cis* N(O)–Fe–N(O) angles) was calculated to compare the structural distortion of the complexes.[29] As shown in Scheme 1, HL^{1-3} ligands are structurally similar tridentate chelating ligands with the only difference in the substituents on the pyridine group, which are –H, $–CH_3$ and –Br, respectively. As expected, two deprotonated ligands $(L^x)^-$ coordinate to the iron(II) ion in an enolic form and lead to a $Fe^{II}N_4O_2$ octahedral coordination environment (Fig. 1). A similar $Fe^{II}N_4O_2$ coordination geometry is favorable for achieving spin crossover in these complexes.[30–41]

According to the crystal data at 173 K, complexes **1·2ACE–3·2ACE** are isomorphous and all crystallize in the monoclinic

Table 1 Crystal data for complexes

	1·2ACE	**2·2ACE**		**3·2ACE**	**4·6H$_2$O**	
Formula	$C_{52}H_{40}FeN_6O_4$	$C_{54}H_{44}FeN_6O_4$		$C_{52}H_{38}Br_2FeN_6O_4$	$C_{50}H_{48}FeN_6O_8$	
Formula weight	868.75	896.80		1026.55	916.79	
T (K)	173	100	173	173	100	220
Crystal system	Monoclinic	Monoclinic	Monoclinic	Monoclinic	Tetragonal	Tetragonal
Space group	$P2_1/c$	$P2_1/c$	$P2_1/c$	$P2_1/c$	$I4_1/a$	$I4_1/a$
a (Å)	16.7076(4)	16.9572(5)	17.2074(4)	17.1295(3)	15.6690(6)	15.7568(8)
b (Å)	8.9821(2)	8.8976(2)	8.9066(2)	8.9127(2)	15.6690(6)	15.7568(8)
c (Å)	28.5746(9)	29.1652(7)	29.2566(7)	29.6320(5)	37.8269(19)	38.012(2)
α (°)	90	90	90	90	90	90
β (°)	95.696(2)	95.151(2)	94.976(2)	94.632(2)	90	90
γ (°)	90	90	90	90	90	90
V (Å^3)	4267.00(19)	4382.63(19)	4466.95(18)	4509.15(15)	9287.2(9)	9437.5(11)
Z	4	4	4	4	8	8
ρ_{calc} (g cm^{-3})	1.352	1.359	1.334	1.456	1.311	1.138
μ (mm^{-1})	3.277	3.207	3.146	5.192	0.368	0.362
F (000)	1808	1872	1872	1929	3840	3360
Data/restraints/parameters	7180/0/572	7190/0/592	7490/0/603	7597/0/589	5536/0/267	5614/0/269
GOF on F^2	1.176	1.067	1.283	1.016	0.938	1.068
R_1 [$I > 2\sigma(I)$]	0.0489	0.0486	0.0553	0.054	0.0886	0.0969
wR_2 (all data)	0.0997	0.115	0.1429	0.1305	0.2270	0.3003
CCDC	2338650	2338649	2338648	2338647	2338646	2338645

Table 2 Selected bond distances (Å) and bond angles (°) for the complexes

Complexes	**1·2ACE**	**2·2ACE**		**3·2ACE**	**4·6H$_2$O**	
T/K	173	100	173	173	100	220
Fe(1)–N(1)	1.951(3)	2.107(3)	2.215(3)	2.277(4)	2.220(4)	2.235(4)
Fe(1)–N(2)	1.862(2)	1.966(3)	2.083(3)	2.091(3)	2.069(4)	2.079(4)
Fe(1)–N(5)	1.860(2)	1.964(3)	2.072(3)	2.103(3)	2.069(4)	2.079(4)
Fe(1)–N(4)	1.959(3)	2.139(3)	2.250(3)	2.251(3)	2.220(4)	2.234(4)
Fe(1)–O(1)	1.955(2)	1.995(2)	2.061(3)	2062(3)	2.084(3)	2.090(3)
Fe(1)–O(2)	1.971(2)	2.027(3)	2.092(3)	2091(3)	2.084(3)	2.090(3)
N(5)–Fe(1)–N(2)	176.73(12)	169.45(10)	168.43(13)	167.00(13)	166.4(2)	166.4(2)
O(1)–Fe(1)–N(4)	161.82(10)	154.89(11)	148.19(13)	146.70(12)	148.68(13)	147.42(14)
O(2)–Fe(1)–N(1)	161.53(10)	154.29(11)	168.43(13)	147.05(13)	148.68(13)	147.42(14)
Σ (°)	82.4	113.6	144.5	150.4	154.9	182.1

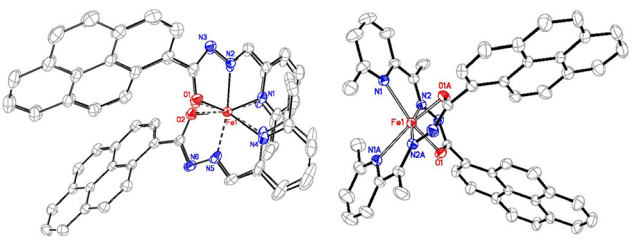

Fig. 1 Left panel: crystal structure of complex **2·2ACE** at 100 K (hollow line) and 173 K (solid line). Right panel: crystal structure of complex **4·6H$_2$O**. Hydrogen atoms are omitted for clarity.

$P2_1/c$ space group with the general formula $Fe^{II}(L^x)_2$·2ACE. Complex **4·6H$_2$O** crystallizes in the $I4_1/a$ space group with the formula $Fe^{II}(L^4)_2$·6H$_2$O. The coordination bond lengths and angles of the central iron(II) ions in these three complexes can be used to determine their spin states.[42–44]

At 173 K, the average coordination bond lengths of Fe–N_{imine} and Fe–N_{py} in complex **1·2ACE** are 1.861 and 1.955 Å, and that of Fe–O_{av} is 1.963 Å. The Fe–N_{imine} bond length is significantly shorter than Fe–N_{py} in the Schiff base hydrazone structures, and can be used as an indicator for judging the spin state of the Fe(II) center.[45] The N_{imine}–Fe–N_{imine} bond angle of 176.73(12)° is close to the ideal value of 180° for low-spin Fe(II) complexes, indicating that iron(II) ions in complex **1·2ACE** are in a low spin state at 173 K. In contrast, complex **3·2ACE** has a long Fe–N_{imine} bond length of 2.097 Å, Fe–N_{py} of 2.264 Å and 2.077 Å (Fe–O_{av}) at 173 K. And the N_{imine}–Fe–N_{imine} angle (167.00(13)°) deviates significantly from 180° for low spin iron(II) ions. These results indicate that the iron(II) ions in complex **3·2ACE** should be in a high spin state at 173 K.

Similarly, the iron(II) ions in complex **2·2ACE** should also be high spin (HS) at 173 K with a Fe–N_{imine} bond length of 2.078 Å, Fe–N_{py} of 2.233 Å and Fe–O_{av} of 2.077 Å as well as the N_{imine}–Fe–N_{imine} bond length of 168.43(13)°. The crystal data of complex **2·2ACE** at 100 K show that the space group remains unchanged. The Fe–N_{imine}, Fe–N_{py} and Fe–O_{av} bond lengths decrease to 1.965 Å, 2.123 Å and 2.011 Å, which is slightly higher than the typical value of low spin Fe(II) complexes. The N_{imine}–Fe–N_{imine} bond angle increases to 169.45(10)°. At the same time, its unit cell volume decreased from 4466.95 Å^3 at 173 K to 4382.63 Å^3 at 100 K, with a reduction of 1.89%. This

indicates that the temperature dropped from 173 K to 100 K, triggering an incomplete spin transition for the iron(II) ions in complex **2·2ACE**, which was confirmed by subsequent magnetic measurements. In addition, the Σ value increased by approximately 30° from 100 K to 173 K, indicating that the transition to the high spin state is accompanied by increasing distortion of the octahedral structure. As shown in Fig. 1, the biggest difference is the displacement of the pyridine group of the $(L^2)^-$ accompanying spin transition.

When the measurement temperature drops from 220 K to 100 K, the apparent changes of the coordination bond lengths, bond angles and cell volume in complex **4·6H$_2$O** are consistent with the occurrence of incomplete spin crossover in this temperature range. It is worth mentioning that the 100 K data seem more like high spin than low spin, and this is due to the existence of 54% high spin Fe(II) at 100 K based on the magnetic measurements (*vide post*). The Solvent Mask routine of the Olex2 software was implemented to remove the contributions of disordered solvents in complex **4·6H$_2$O**.[46] A total count of 477 electrons per unit cell was estimated, corresponding to six H_2O per formula unit.

In complexes **1–4·*xsol***, apparent intermolecular C–H···π interactions between the pyrene groups are observed instead of π···π contact, connecting adjacent Fe$(L^x)_2$ molecules to form a one-dimensional chain for **1–3·2ACE** and a 2D layer for complex **4·6H$_2$O** (Fig. S4 and S5, ESI‡). The nearest intermolecular Fe···Fe separations at 173 K are 8.365 Å for **1·2ACE**, 8.440 Å for **2·2ACE**, 8.325 Å for **3·2ACE** and 8.008 Å for **4·6H$_2$O** (100 K), respectively.

Magnetic properties

The variable-temperature direct current magnetic susceptibilities of complexes **1–4·*xsol*** were measured under an applied field of 1000 Oe, and the data are shown as χ_mT *vs.* T plots in Fig. 2. The similarity in the structure of complexes **1·2ACE–3·2ACE** makes it beneficial for studying the substituent effect.

Complex **1·2ACE** is basically in a low spin state even at room temperature, and the small χ_mT value of 1.03 cm^3 K mol^{-1} at 300 K indicates the presence of approximately 27% of high spin Fe(II) centers. The χ_mT value of complex **3·ACE** at 300 K is 3.68 cm^3 K mol^{-1}, which is consistent with the theoretical value for iron(II) ions in the high spin state. During the reduction in temperature up to 50 K, the χ_mT value remains approximately constant. The rapid decrease to 2.88 cm^3 K mol^{-1} at 10 K may be due to intermolecular antiferromagnetic interactions and/or zero-field splitting (ZFS) of HS iron(II) ions. The magnetic data are well consistent with the crystal data.

Complexes **2** and **4·6H$_2$O** exhibit a gradual and incomplete spin-crossover behavior. The χ_mT values remain almost constant from 3.26 cm^3 K mol^{-1} (**2**) and 3.72 cm^3 K mol^{-1} (**4·6H$_2$O**) at 300 K to 175 K (**2**) and 250 K (**4·6H$_2$O**), corresponding to HS iron(II) ions in this temperature range. As the temperature further decreases, the χ_mT value drops regularly to 1.58 cm^3 K mol^{-1} at 75 K for complex **2** and to 2.23 cm^3 K mol^{-1} at 125 K for complex **4·6H$_2$O**. This corresponds to the existence of 48.5% and 60.0% residual HS Fe(II) in complexes **2** and **4·6H$_2$O**, respectively. The magnetic measurements for the warming and cooling process show no thermal hysteresis effect, which is understandable for such gradual SCO complexes.

In general, similar complexes **1·2ACE**, **2**, **3·ACE** show different magnetic properties in the testing temperature range: low spin complex **1·2ACE**, spin crossover complex **2** and high spin complex **3·ACE**. Substituting groups R, in the *ortho* position of coordinating pyridine N atom, are –H, –CH$_3$ and –Br in complexes **1–3·2ACE**, respectively. The electron-donating ability and steric hindrance of the substituents are expected to affect the ligand field strength of the Fe(II) complexes. The order of electron-donating ability of the three substituents is HL^2 (R = CH_3) > HL^1 (R = H) > HL^3 (R = Br), and the order of steric hindrance is HL^2 (R = CH_3) > HL^3 (R = Br) > HL^1 (R = H). The combined effect of these two factors leads to the ligand field strength in the order of HL^1 (R = H) > HL^2 (R = CH_3) > HL^3 (R = Br), as evidenced by DFT calculations on analogous rhodamine 6G pyridylhydrazone Fe(II)N_4O_2 complexes.[45] This work reemphasizes the effective substituent strategy of modifying the ligand field strength and spin states.

The spin transition temperature ($T_{1/2}$ = 180 K) of complex **4·6H$_2$O** is higher than that of complex **2** ($T_{1/2}$ = 120 K), as shown in Fig. 2. The substitution of R′ (CH_3 for complex **4·6H$_2$O**, H for complex **2**, Scheme 1) is another way to tune the spin state. The present result indicates that changing the substituent R′ from H atom to methyl leads to the enhancement of ligand field strength to some extent.

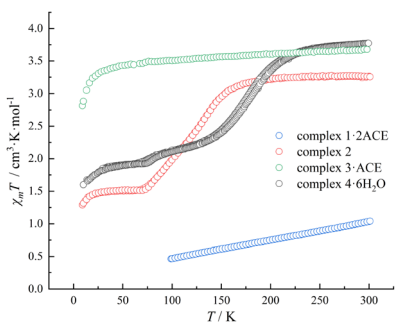

Fig. 2 Temperature dependence of χ_mT for complexes **1·2ACE**, **2**, **3·ACE** and **4·6H$_2$O**.

Fluorescence spectroscopy

In order to investigate the coupling effect between the magnetic properties and fluorescence properties of complexes **2** and **4·6H$_2$O**, the solid-state temperature-dependent fluorescence of complexes **2** and **4·6H$_2$O** was measured. As shown in Fig. 3, the maximum fluorescence intensity of complex **2** decreases monotonically with increasing temperature over the whole temperature range (80–250 K), which is caused by the thermal quenching effect. This indicates that complex **2** has no correlation between the spin transition and fluorescence.

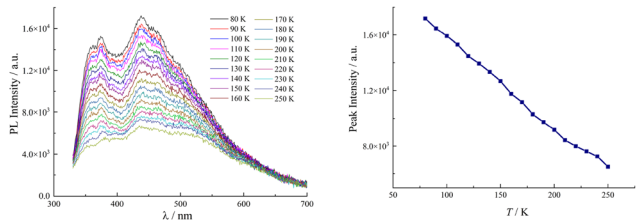

Fig. 3 Left panel: temperature-dependent emission spectra of complex **2** (λ_{ex} = 300 nm). Right panel: the fluorescence intensity of the maximum emission (λ_{em} = 438 nm) for complex **2**.

The temperature-dependent photoluminescence of complex **4·6H$_2$O** (Fig. 4) is slightly different from complex **2**. In the temperature range of 300–200 K, the maximum fluorescence emission intensity of complex **4·6H$_2$O** decreases linearly with the increase of temperature, which is similar to that of complex **2**. In the range of 200–100 K, the change in maximum fluorescence emission intensity is not obvious, and the intensities fluctuate.

To ascertain whether this anomaly is due to the coupling effect between the magnetic and fluorescence properties of complex **4·6H$_2$O**, we measured the solid-state temperature-dependent fluorescence of ligand HL^4 (Fig. S6, ESI‡). The emission intensity of HL^4 is significantly stronger than complex **4·6H$_2$O**, reflecting the quenching effect of iron(II) ions on the fluorescence. However, the trend of HL^4 fluorescence intensity changing with temperature is basically consistent with that of complex **4·6H$_2$O** (Fig. 4), indicating that there is no coupling effect between the fluorescence properties and spin crossover behavior of the complex.

Therefore, complexes **2** and **4·6H$_2$O** do not display the fluorescence–SCO coupling effect, which seems strange given that a few pyrene-based SCO Fe(II) complexes show the coupling effect.[18,20,24,26,27] It is probably due to the short distance between the Fe(II) center and the pyrene fluorophore of the coordinating ligands in complexes **2** and **4·6H$_2$O** favoring non-radiative energy transfer.[47,48] In addition, the gradual spin crossover behavior of complexes **2** and **4·6H$_2$O** is another disadvantage affecting the coupling effect although there are some complexes showing gradual SCO and the coupling effect.[49–51]

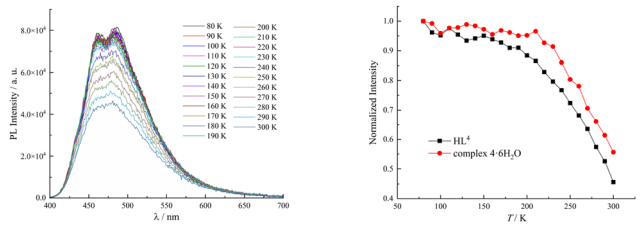

Fig. 4 Left panel: temperature-dependent emission spectra of complex **4·6H$_2$O** (λ_{ex} = 350 nm). Right panel: the normalized fluorescence intensity of the peak emission (λ_{em} = 463 nm) for complex **4·6H$_2$O** and HL^4.

Conclusions

In summary, we have designed and synthesized four neutral mononuclear Fe(II) complexes based on new tridentate Schiff base-type ligands with a pyrene fluorophore. Complexes **1·2ACE** (R = H), **2** (R = CH_3) and **3·ACE** (R = Br) exhibit low spin, spin crossover, and high spin state in the testing temperature range, respectively, reflecting the significant influence of the substituent R on the magnetic properties. Complex **4·6H$_2$O** (R = R′ = CH_3) shows spin-crossover properties with a higher transition temperature than complex **2**. The temperature dependent fluorescence emission spectra show that the emission intensity of complexes **2** and **4·6H$_2$O** is independent of their spin-crossover behavior. Therefore, the magnetism of the fluorescent Fe(II) complexes can be tuned by the substituents at specific positions, providing an effective strategy for the controllable synthesis of multifunctional magnetic materials.

Author contributions

X. W. synthesized the sample, performed the PXRD analysis and fluorescence and magnetic measurements, and wrote the paper. N.Z. grew the single crystals and performed the single-crystal studies. H.-Z.K. supervised the study. All authors discussed the results and commented on the paper.

Data availability

The data that support the findings of this study are available in the ESI‡ of this article. The crystallographic data for the structures reported in this article have been deposited at the Cambridge Crystallographic Data Centre under deposition numbers CCDC 2338645–2338650.‡

Conflicts of interest

There are no conflicts to declare.

Acknowledgements

This work was supported by the National Natural Science Foundation of China (Project No. 22271171, 22101076 and 21971142).

References

1 P. Gütlich, Y. Garcia and H. A. Goodwin, *Chem. Soc. Rev.*, 2000, **29**, 419–427.
2 J. A. Real, A. B. Gaspar and M. C. Muñoz, *Dalton Trans.*, 2005, **12**, 2062–2079.
3 B. Sally, *Chem. Soc. Rev.*, 2015, **44**, 2880–2892.

4 Z.-P. Ni, J.-L. Liu, N. Hoque, W. Liu, J.-Y. Li, Y.-C. Chen and M.-L. Tong, *Coord. Chem. Rev.*, 2017, **335**, 28–43.
5 O. Kahn and C. J. Martinez, *Science*, 1998, **279**, 44–48.
6 J. Linares, E. Codjovi and Y. Garcia, *Sensors*, 2012, **12**, 4479–4492.
7 E. Coronado, *Nat. Rev. Mater.*, 2020, **5**, 87–104.
8 H. Phan, S. M. Benjamin, E. Steven, J. S. Brooks and M. Shatruk, *Angew. Chem., Int. Ed.*, 2015, **54**, 823–827.
9 D. Shao, L. Shi, L. Yin, B.-L. Wang, Z.-X. Wang, Y.-Q. Zhang and X.-Y. Wang, *Chem. Sci.*, 2018, **9**, 7986–7991.
10 A. B. Gaspar, V. Ksenofontov, M. Seredyuk and P. Gütlich, *Coord. Chem. Rev.*, 2005, **249**, 2661–2676.
11 B. Benaicha, K. V. Do, A. Yangui, N. Pittala, A. Lusson, M. Sy, G. Bouchez, H. Fourati, C. J. Gómez-García, S. Triki and K. Boukheddaden, *Chem. Sci.*, 2019, **10**, 6791–6798.
12 B. Rösner, M. Milek, A. Witt, B. Gobaut, P. Torelli, R. H. Fink and M. M. Khusniyarov, *Angew. Chem., Int. Ed.*, 2015, **54**, 12976–12980.
13 J. Yuan, S.-Q. Wu, M.-J. Liu, O. Sato and H.-Z. Kou, *J. Am. Chem. Soc.*, 2018, **140**, 9426–9433.
14 K. Sun, J.-P. Xue, Z.-S. Yao and J. Tao, *Dalton Trans.*, 2022, **51**, 16044–16054.
15 H. J. Shepherd, C. M. Quintero, G. Molńar, L. Salmon and A. Bousseksou, in *Spin-Crossover Materials: Properties and Application*, ed. M. A. Halcrow, John Wiley & Sons Ltd, 2013, pp. 347–373.
16 M. K. Javed, A. Sulaiman, M. Yamashita and Z.-Y. Li, *Coord. Chem. Rev.*, 2022, **467**, 214625.
17 K. S. Kumar and M. Ruben, *Coord. Chem. Rev.*, 2017, **346**, 176–205.
18 H. Matsukizono, K. Kuroiwa and N. Kimizuka, *Chem. Lett.*, 2008, **37**, 446–447.
19 S. Titos-Padilla, J. M. Herrera, X. W. Chen, J. J. Delgado and E. Colacio, *Angew. Chem., Int. Ed.*, 2011, **50**, 3290–3293.
20 C.-F. Wang, R.-F. Li, X.-Y. Chen, R.-J. Wei, L.-S. Zheng and J. Tao, *Angew. Chem., Int. Ed.*, 2015, **54**, 1574–1577.
21 I. Suleimanov, O. Kraieva, G. Molnár, L. Salmon and A. Bousseksou, *Chem. Commun.*, 2015, **51**, 15098–15101.
22 C. F. Wang, G. Y. Yang, Z. S. Yao and J. Tao, *Chem. – Eur. J.*, 2018, **24**, 3218–3224.
23 R. González-Prieto, B. Fleury, F. Schramm, G. Zoppellaro, R. Chandrasekar, O. Fuhr, S. Lebedkin, M. Kappes and M. Ruben, *Dalton Trans.*, 2011, **40**, 7564–7570.
24 J.-L. Wang, Q. Liu, Y.-S. Meng, X. Liu, H. Zheng, Q. Shi, C.-Y. Duan and T. Liu, *Chem. Sci.*, 2018, **9**, 2892–2897.
25 B. X. Luo, Y. Pan, Y. S. Meng, Q. Liu, J. Yin, T. Liu and Y. Y. Zhu, *Eur. J. Inorg. Chem.*, 2021, 3992–3999.
26 I. Suleimanov, O. Kraieva, J. S. Costa, I. O. Fritsky, G. Molnár, L. Salmon and A. Bousseksou, *J. Mater. Chem. C*, 2015, **3**, 5026–5032.
27 T. Delgado, M. Meneses-Sánchez, L. Piñeiro-López, C. Bartual-Murgui, M. C. Muñozc and J. A. Real, *Chem. Sci.*, 2018, **9**, 8446–8452.
28 H. Ryu, J. H. Baek, M. G. Choi, J. C. Lee and S. K. Chang, *Tetrahedron Lett.*, 2017, **58**, 2927–2930.
29 P. Guionneau, M. Marchivie, G. Bravic, J. F. Létard and D. Chasseau, *Top. Curr. Chem.*, 2004, **234**, 97–128.
30 G. Psomas, N. Bréfuel, F. Dahan and J. P. Tuchagues, *Inorg. Chem.*, 2004, **43**, 4590–4594.
31 L. Zhang, G. C. Xu, H. B. Xu, T. Zhang, Z. M. Wang, M. Yuan and S. Gao, *Chem. Commun.*, 2010, **46**, 2554–2556.
32 B. Weber, *Coord. Chem. Rev.*, 2009, **253**, 2432–2449.
33 T. Romero-Morcillo, M. Seredyuk, M. C. Muñoz and J. A. Real, *Angew. Chem., Int. Ed.*, 2015, **54**, 14777–14781.
34 D. Rosario-Amorin, P. Dechambenoit, A. Bentaleb, M. Rouzières, C. Mathonière and R. Clérac, *J. Am. Chem. Soc.*, 2018, **140**, 98–101.
35 B. Dey and V. Chandrasekhar, *Dalton Trans.*, 2022, **51**, 13995–14021.
36 T. Nakanishi, Y. Hori, H. Sato, S.-Q. Wu, A. Okazawa, N. Kojima, T. Yamamoto, Y. Einaga, S. Hayami, Y. Horie, H. Okajima, A. Sakamoto, Y. Shiota, K. Yoshizawa and O. Sato, *J. Am. Chem. Soc.*, 2019, **141**, 14384–14393.
37 M. S. Shongwe, S. H. Al-Rahbi, M. A. Al-Azani, A. A. Al-Muharbi, F. Al-Mjeni, D. Matoga, A. Gismelseed, I. A. Al-Omari, A. Yousif, H. Adams, M. J. Morris and M. Mikuriya, *Dalton Trans.*, 2012, **41**, 2500–2514.
38 Y.-S. Ye, X.-Q. Chen, K.-Y. Shen, M.-L. Tong and X. Bao, *CCS Chem.*, 2020, **2**, 2350–2358.
39 J. Kusz, M. Nowak and P. Gütlich, *Eur. J. Inorg. Chem.*, 2013, 832–842.
40 C. Lochenie, K. Schötz, F. Panzer, H. Kurz, B. Maier, F. Puchtler, S. Agarwal, A. Köhler and B. Weber, *J. Am. Chem. Soc.*, 2018, **140**, 700–709.
41 O. Iasco, E. Riviere, R. Guillot, M. B.-L. Cointe, J.-F. Meunier, A. Bousseksou and M.-L. Boillot, *Inorg. Chem.*, 2015, **54**, 1791–1799.
42 L. Zhang, G. C. Xu, H. B. Xu, V. Mereacre, Z. M. Wang, A. K. Powell and S. Gao, *Dalton Trans.*, 2010, **39**, 4856–4868.
43 M. A. Halcrow, *Chem. Soc. Rev.*, 2011, **40**, 4119–4142.
44 O. G. Shakirova and L. G. Lavrenova, *Crystals*, 2020, **10**, 843.
45 J. Yuan, M.-J. Liu, S.-Q. Wu, X. Zhu, N. Zhang, O. Sato and H.-Z. Kou, *Inorg. Chem. Front.*, 2019, **6**, 1170–1176.
46 B. Rees, L. Jenner and M. Yusupov, *Acta Crystallogr., Sect. D: Biol. Crystallogr.*, 2005, **61**, 1299–1301.
47 C. Lochenie, K. G. Wagner, M. Karg and B. Weber, *J. Mater. Chem. C*, 2015, **3**, 7925–7935.
48 M. Meneses-Sánchez, L. Piñeiro-López, T. Delgado, C. Bartual-Murgui, M. C. Muñoz, P. Chakraborty and J. A. Real, *J. Mater. Chem. C*, 2020, **8**, 1623–1633.
49 X.-R. Wu, Z.-K. Liu, M. Zeng, M.-X. Chen, J. Tao, S.-Q. Wu and H.-Z. Kou, *Sci. China: Chem.*, 2022, **65**, 1569–1576.
50 Y. R. Qiu, L. Cui, J. Y. Ge, M. Kurmoo, G. Ma and J. Su, *Front. Chem.*, 2021, **9**, 692939.
51 X.-R. Wu, S.-Q. Wu, Z.-K. Liu, M.-X. Chen, J. Tao, O. Sato and H.-Z. Kou, *Nat. Commun.*, 2024, **15**, 3961.

